

Quantifying temperature-induced magnetic disorder effects on the anisotropy of MnBi

Christopher E. Patrick

*Department of Materials, University of Oxford, Parks Road, Oxford OX1 3PH, UK**

(Dated: July 4, 2022)

MnBi is remarkable for having a magnetocrystalline anisotropy (MCA) which increases with temperature. This unusual behavior has been attributed to the thermal expansion of the lattice and, more recently, to an anisotropic vibrational free energy. However, the effect of magnetic fluctuations on the MCA has not yet been quantified. Here, first-principles density-functional theory calculations based on the disordered local moment picture (DFT-DLM) are used to calculate the MCA of MnBi in the presence of magnetic disorder. The MCA is obtained from the magnetic torque, calculated as a function of magnetization angle and temperature T . At fixed ionic positions, the MCA decays monotonically with increasing T . The DFT-DLM torques provide access to the individual anisotropy constants κ_l (which parametrize the relation between magnetic energy and magnetization angle), and their dependence on order parameter m . The lowest order constant κ_2 follows single-ion like behavior at low T but decays as m^4 as T increases, while the higher order constants deviate strongly from single-ion predictions. Zero- T calculations show that a spin reorientation transition can be triggered by removing 0.1 electrons, resulting in c -axis magnetization once 0.25 electrons have been removed. The zero-temperature calculations are cross-validated using an alternative implementation of DFT based on wavefunctions, plane waves and pseudopotentials.

I. INTRODUCTION

With a room temperature magnetization of 0.6 MA m^{-1} and ferromagnetic order which persists up to 630 K [1], MnBi is an interesting example of a permanent magnet material which contains neither rare earths nor the elemental ferromagnets Fe, Co or Ni [2]. From a theoretical point of view, MnBi is particularly intriguing due to the way its magnetocrystalline anisotropy (MCA) evolves with temperature. The easy direction of magnetization lies in the ab plane at 4 K but points along the c -axis at room temperature [3]. The change in magnetization direction occurs as a spin reorientation transition (SRT) which begins at ~ 90 K with a sudden flop from the ab plane to an easy angle oriented $\lesssim 40^\circ$ to the c axis [4]. As the temperature increases, the easy direction rotates steadily towards c and the SRT completes at 140 K [4]. MnBi then displays uniaxial (c -axis) anisotropy up to 630 K. This SRT behavior has been observed independently in neutron scattering [3, 5], NMR [4] and magnetization [6] experiments [7].

At temperatures above the SRT, MnBi displays an unusual phenomenon whereby its MCA energy increases with temperature [6]. Since MnBi is hexagonal, fundamental symmetry considerations provide an expression for the dependence of the free energy F on the angle θ between the magnetization direction and the c -axis:

$$F(\theta) = K_1 \sin^2 \theta + K_2 \sin^4 \theta + K_3 \sin^6 \theta \quad (1)$$

Equation 1 has been truncated at $\sin^6 \theta$ and neglects any anisotropy in the basal plane, which will be justified later.

The energy difference between c -axis and ab -plane magnetization ($\theta = 0$ or 90°) is $K_{\text{tot}} = K_1 + K_2 + K_3$. The authors of Ref. [6] performed magnetization measurements for fields applied parallel and perpendicular to c , and fitted their data by minimizing the sum of F and the Zeeman energy. The extracted K_{tot} increases linearly with temperature up to 400 K, reaches a peak at a value of 3.1 MJ m^{-3} at 460 K, and then reduces rapidly [6].

MnBi's increasing MCA with temperature has long been identified as an interesting phenomenon, appearing in Kittel's 1949 review [8]. The magnetism originates from the Mn atoms, with neutron scattering finding local magnetic moments of 3.9 Bohr magnetons (μ_B) at the Mn sites at 5 K [5]. At absolute zero, these local moments will be fully ordered and ferromagnetically aligned, but increasing the temperature provides the thermal energy required to access microstates where the local moments are disordered [9]. This effect is conveniently described using unit vectors $\hat{\mathbf{e}}_i$ to denote the orientation of a local moment i in a particular microstate, and $\mathbf{m}_i = \langle \hat{\mathbf{e}}_i \rangle_T$ to denote its thermally-averaged orientation at a temperature T . \mathbf{m}_i is the order parameter, whose magnitude varies from 1 in the zero- T ferromagnetic state, to 0 above the Curie temperature in the paramagnetic state.

Generally, we expect individual contributions to the anisotropy to reduce with m_i , and therefore to decrease with increasing T . For instance, Callen-Callen theory yields characteristic decay laws to describe the MCA generated by isolated moments (single ions) [10, 11]. Furthermore, both the MCA due to dipolar interactions between pairs of local moments [12] and also the MCA of metallic ferromagnets like FePt decay proportional to m_i^2 [13, 14]. However, even if individual contributions to the MCA exhibit monotonic decay with temperature, adding them together may produce a total anisotropy which is non-monotonic. One example is NdCo₅, where the total anisotropy is a competition between the Nd

* christopher.patrick@materials.ox.ac.uk

(planar) and Co (uniaxial) contributions [15]. $\text{Y}_2\text{Fe}_{14}\text{B}$ is another material with multiple magnetic sublattices whose total MCA increases with temperature, although the origin of this effect is less clear [16]. But even a single-ion description of one magnetic sublattice can yield a non-monotonic MCA [11]. Equation 1 can be rewritten in terms of the Legendre polynomials $P_l(x)$ as

$$F(\theta) = (\kappa_2 + \kappa_4 + \kappa_6) + \kappa_2 P_2(\cos \theta) + \kappa_4 P_4(\cos \theta) + \kappa_6 P_6(\cos \theta) \quad (2)$$

where equating coefficients of $\cos^l \theta$ gives relations between K_i and κ_l , e.g. $K_1 = -\frac{3}{2}\kappa_2 - 5\kappa_4 - \frac{21}{2}\kappa_6$ [17]. Single-ion theory predicts that the κ_l coefficients decay monotonically with temperature, at rates depending on l [10]. But if these coefficients have different signs, combining them will produce K_i values with non-monotonic decay. This is the mechanism believed to drive the low-temperature SRT in $\text{Nd}_2\text{Fe}_{14}\text{B}$ [18].

The above discussion focuses on how temperature can directly affect the MCA, by introducing magnetic disorder. Indeed, the authors of Ref. [12] showed how the temperature dependence of the anisotropy constants of MnBi could be explained very satisfactorily in terms of a phenomenological spin model in the spirit of Callen-Callen theory. However, increasing the temperature will also provide energy for ionic motion, and this may affect the MCA. First, anharmonicity in the potential energy landscape will lead to thermal expansion. Second, the free energy will gain another contribution associated with the vibrational excitations (phonons). Accounting for these factors modifies the free energy expression:

$$F_{\text{tot}}(\theta, T) = F_a(\theta, m, \tau) + F_{\text{vib}}(\theta, m, \tau, T) \quad (3)$$

In equation 3, τ has been used to label schematically the unit cell vectors and ionic positions at equilibrium, and m the order parameters of the magnetic atoms. F_a represents the free energy depending on magnetic disorder as discussed above, but now it is made explicit that the ions are clamped at positions τ . F_{vib} is the free energy associated with phonons, discussed more below. Assuming τ remains consistent with hexagonal symmetry, F_{tot} obeys equation 1, and the anisotropy constants will in principle contain contributions from F_a and F_{vib} .

In the harmonic approximation, F_{vib} is given by [19]

$$F_{\text{vib}} = \sum_{\nu} \left[\frac{\hbar \omega_{\nu}}{2} + k_B T \ln \left[1 - e^{-\hbar \omega_{\nu} / (k_B T)} \right] \right] \quad (4)$$

where ω_{ν} are the phonon frequencies. These depend on the equilibrium positions τ (e.g. in the quasiharmonic approximation, it is the volume dependence of ω_{ν} which leads to thermal expansion [19]), but equation 3 also permits that ω_{ν} depends on the magnetization direction θ and the degree of magnetic order m . The θ -dependence is believed to be crucial to MnBi, as discussed below [20]. The m -dependence has been illustrated in other materials, e.g. in calculations of the phonon spectra for ferromagnetic and paramagnetic bcc Fe [21]. Conceptually,

this picture assumes a Born-Oppenheimer-like separation between faster magnetic and slower vibrational excitations, such that the forces on ions are determined from a thermal average of magnetic microstates [22].

Equation 3 demonstrates the potential complexity of understanding the temperature dependence of the MCA, if there is coupling between the magnetism and ionic positions. This is because temperature enters explicitly in F_{vib} and implicitly through $m(T)$, $\tau(T)$ and $\omega(m(T), \tau(T))$. Previous studies, experimental and theoretical, have found that this coupling is indeed strong in MnBi [5, 20, 23–28]. On the experimental side, evidence is provided by observing the correlation between structural parameters and magnetization (magnetostriction), particularly through the SRT [5, 23, 24]. Theoretical evidence has been obtained through first-principles density-functional theory (DFT) calculations. Ref. [25] reported that the clamped-ion MCA was sensitive to homogeneous deformation of the unit cell volume. The authors of Ref. [26] went further and showed how, by taking the temperature-dependent lattice constants from experiment [24] and calculating the clamped-ion MCA within the local spin-density approximation including a Hubbard U correction (LSDA+ U) [29], they were able to reproduce the experimentally-reported K_{tot} [6] with an accuracy better than 0.1 meV/cell over a temperature range of 100–450 K. Ref. [30] also showed that distorting the lattice could account for the SRT once a Hubbard U correction was included. These results imply that F_a accounts completely for T -dependence of the MCA and any contribution from F_{vib} is negligible. However, Ref. [27] found using a generalized-gradient approximation (DFT-GGA [31]) that the MCA was sensitive to atomic displacements even when the unit cell volume was held constant, and argued that approximately 64% of the change in MCA with temperature could be accounted for by vibrational motion alone. Most recently, the authors of Ref. [20] applied their development of a relativistic, magnetic generalization of density-functional perturbation theory (DFPT) [32] to calculate F_{vib} for magnetization along the c or a -axes within the LSDA [33]. They found the contribution to the MCA from F_{vib} to be positive (0.5 meV/cell at $T = 0$ K) and to increase with temperature at a rate similar to that observed experimentally for K_{tot} [6]. Combining this contribution with that from F_a (calculated within DFT-GGA [31], using experimentally-obtained lattice expansion on top of DFT-GGA optimized lattice vectors), yielded agreement with the experimentally-measured K_{tot} at a similar or improved level to Ref. [26], again up to 450 K.

Ref. [20] provides arguably the most complete explanation of the temperature-dependent MCA of MnBi to date, taking into account both thermal expansion and vibrational motion. However, like in all of the works described above [25–28, 30], the calculations of Ref. [20] were performed for the fully-ordered, ferromagnetic state, i.e. $m = 1$. The T -dependence of F_{tot} obtained in those works derives from F_a depending on $\tau(T)$ and (for

Ref. [20]) F_{vib} depending explicitly on T . To this author's knowledge there have been no attempts to quantify from first principles the effect of magnetic disorder on the MCA of MnBi, i.e. obtain the m dependence of F_a . This is an important gap, particularly in light of the success of the spin model of Ref. [12] in describing the temperature evolution of the anisotropy constants.

The current study seeks to address this aspect. Treating magnetic disorder within the relativistic density-functional theory implementation of the disordered local moment picture (DFT-DLM) [9, 34], the temperature evolution of the magnetic order parameters and the angular dependence of the free energy have been calculated from first principles, allowing the extraction of the MCA as a function of T . In particular, the study takes advantage of recent methodological developments [35] which enable access to the individual anisotropy constants K_1 , K_2 and K_3 , thus going beyond previous studies which obtained the unresolved quantity K_{tot} . Zero- T calculations have also been performed to show the influence of hole doping on the anisotropy constants, and also to compare different implementations of DFT, either in Korringa-Kohn-Rostocker (KKR) multiple-scattering theory [36] or in the plane wave and pseudopotential formalism [37].

It is important to state at the outset that all calculations have been performed for clamped ions, so that only the contribution from F_a has been calculated. Furthermore, for the majority of the calculations τ has been fixed to its zero- T value, so that the temperature evolution of the MCA derives entirely from m . This work is therefore intended to complement, rather than supplant, previous studies, which fixed m and focused on the evolution of the MCA with τ . In light of the missing contributions from F_{vib} it is not to be expected that the calculated anisotropy constants will reproduce experimental values. However, the current calculations allow a clean separation of the MCA from magnetoelasticity, a luxury which is unavailable in experiments, and provide a first-principles description of the m -dependence of the MCA of this interesting material.

The rest of the manuscript is ordered as follows. Section II describes the methodological approach employed in the study, including the technical details of the different calculations. Section III presents and discusses the results, including at zero and finite temperature (sections III A and III D, respectively). Finally, the conclusions and suggested future directions for study are presented in Section IV.

II. METHODOLOGY

A. Crystal structure

High resolution diffraction measurements performed on single crystals [5] confirmed that MnBi adopts the NiAs structure at room temperature, (space group 194, $P6_3/mmc$, Fig. 1), with Mn and Bi at the $2a$ and $2c$

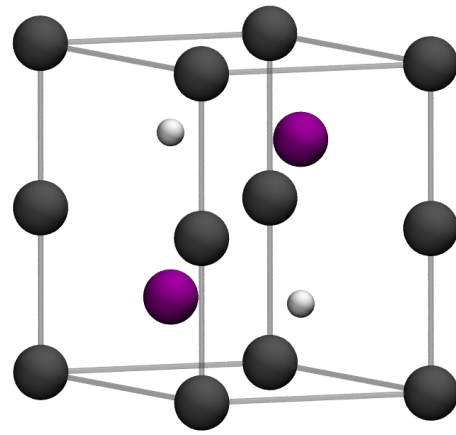


FIG. 1. The NiAs structure of MnBi used in this study. The gray and purple spheres represent Mn and Bi atoms, respectively. The white spheres represent voids at the $2d$ sites where empty spheres were placed in KKR-ASA calculations.

Wyckoff positions respectively. The same experiments found that below 90 K, MnBi undergoes a distortion in the ab plane which lowers the symmetry to $Cmcm$. Whilst this effect is small, (with the ideal angle of 60° reducing to 59.94° at 20 K [5]), the fact that it coincides with the initiation of the SRT forms part of the experimental evidence for the importance of the coupling between magnetism and ionic positions.

As noted in the Introduction, this work aims to quantify the influence of magnetic disorder on the MCA in isolation from magnetoelasticity. For this reason, all calculations presented here use the NiAs structure. In order to reduce the size of the interstitial region, for calculations adopting the atomic sphere approximation (ASA), empty spheres were also placed at the $2d$ sites (Fig. 1). The lattice parameters $a = 4.27$ Å and $c = 6.05$ Å were used for most cases, measured experimentally at 4 K as reported in Ref. [24] (it should be noted that these experiments did not resolve the $Cmcm$ distortion). The reason for using these parameters rather than from other experiments like Ref. [5] is to facilitate comparison to previous theoretical work [20, 26]. A set of calculations presented in Sec. III D used temperature-dependent a and c values, also taken from Ref. [24]. For reference, an anisotropy energy of 1 meV/unit cell is equivalent to 1.67 MJm $^{-3}$ at the 4 K lattice parameters.

B. Zero and finite temperature KKR-ASA calculations

The methodology employed to calculate the MCA at finite temperature [9, 34, 38] has been comprehensively reviewed in a recent article [35], so only the key points will be presented here. The first step is to perform a self-consistent, scalar-relativistic DFT calculation of the fully-ordered (ferromagnetic) state. Here, exchange and

correlation was described within the LSDA [39] and the ground state density and potentials determined within the KKR multiple-scattering formalism of DFT using the atomic sphere approximation (KKR-ASA), as implemented in the HUTSEPOT code [40]. All angular momentum expansions were performed up to a maximum quantum number $l_{\max} = 3$ and reciprocal space sampled on a $20 \times 20 \times 20$ grid. The Wigner-Seitz radii for the atomic spheres were calculated using the protocol described in Appendix A for each set of lattice parameters. As an example, for $a = 4.27$ Å and $c = 6.05$ Å the radii used were 2.92, 3.52 and 2.04 Bohr radii for Mn, Bi and empty spheres, respectively. The magnetic moments (calculated as the integral of the spin density in the atomic spheres) were found to be 3.78 and $-0.19 \mu_B$ for Mn and Bi respectively, the minus sign showing antiferromagnetic alignment.

The second step is to use these atom-centred potentials as inputs to DFT-DLM calculations. The MARMOT code [35] is used to perform these calculations as a post-processing step. Here, the single-site scattering problem is solved fully relativistically [34] and magnetic disorder is treated at the level of the coherent potential approximation (CPA) [36]. The probability that a local moment is oriented along a particular direction $\hat{\mathbf{e}}_i$ is proportional to $\exp[\hat{\mathbf{e}}_i \cdot \mathbf{h}_i / (k_B T)]$. The Weiss fields \mathbf{h}_i are not free parameters, but are provided by solving the DFT-DLM equations at each temperature [9]. Knowledge of the Weiss fields gives the order parameters m_i as a function of temperature through the relation $m_i = L[h_i / (k_B T)]$, where L is the Langevin function.

The MCA is calculated using the torque formalism [41], which provides direct access to the derivative of the DFT-DLM free energy, $T(\theta) = \partial F_a / \partial \theta$ [38]. In this approach, one combines the magnetic force theorem [42] with DFT-DLM statistical mechanics to find a torque expression which depends only on the variation of single-particle eigenvalues (the band contribution) with magnetization direction [38]. Numerically the approach carries a significant advantage, since it focuses on calculating one small number directly (the torque) rather than relying on the difference between two large numbers (the free energy) [41]. Reciprocal space was sampled using an adaptive algorithm [43] and the parameters controlling the complex energy integral [35] were carefully checked to ensure numerical convergence of the MCA and Weiss fields. The electronic temperature appearing in the Fermi-Dirac function was fixed to 300 K, as discussed in Appendix B.

The DFT-DLM calculations also provide access to the spin and orbital magnetic moments, calculated as integrals of the Green's function [35]. However, these moments are not then used to update the atom-centred potentials, i.e. the second step is a one-shot procedure. Although a self-consistent relativistic DFT-DLM scheme was demonstrated in Ref. [44], it carries a prohibitively high computational expense compared to the one-shot torque formalism used here [35].

C. Zero temperature PW-PP calculations

The MCA has also been calculated at zero temperature using a different formulation of DFT, based on expanding the Kohn-Sham wavefunctions and electron density in terms of plane waves and accounting for the core-valence interaction with fully-relativistic, ultrasoft pseudopotentials (PW-PP) [45]. These calculations were performed using the Quantum ESPRESSO software package [37] and pseudopotentials provided in the `pslibrary` versions 0.3.1 and 1.0.0 [45] for Mn and Bi, respectively, following Ref. [20]. The wavefunctions and charge density were expanded up to plane wave cutoff energies of 110 and 440 Ry, and reciprocal space was sampled on a $24 \times 24 \times 24$ non- Γ -centred Monkhorst-Pack grid [46]. The electronic states were occupied according to the first-order Methfessel-Paxton smearing scheme [47] with a smearing parameter η of 0.01 Ry. The convergence of the MCA with reciprocal space sampling and η is discussed more in Appendix B.

The PW-PP calculations provide the self-consistent (SCF) charge density and total energy. The SCF cycle was initialized with the magnetization pointing along the desired angle ($\theta = 0-90^\circ$ in 15° intervals). In all cases the converged SCF magnetization remained pointing along its initial direction, with no constraint applied. Since the primary focus of this work is on temperature effects rather than exchange-correlation functional, only the LSDA [33] or PBEsol (GGA) functional [31] have been considered here, i.e. no Hubbard U corrections have been applied.

III. RESULTS AND DISCUSSION

A. MCA at zero temperature

We consider first the zero temperature magnetic state, where all magnetic moments are collinear and the induced moments on the Bi atoms are antiparallel to the Mn. The fully-relativistic KKR-ASA calculations find a total magnetic moment of $3.78 \mu_B/\text{FU}$ (formula unit), which consists of spin (orbital) contributions of 3.82 (0.13) μ_B for Mn and -0.15 (-0.03) μ_B for Bi, for a -axis magnetization. Repeating the calculation for c -axis magnetization finds essentially identical spin moments but a decrease of $0.016 \mu_B$ in the Mn orbital moment. Altogether the total magnetization can be reasonably well described by the expression $M(\theta) = M_0(1 - p \sin^2 \theta)$, with $M_0 = 3.75 \mu_B/\text{FU}$ and $p = -0.0046$. Whilst definitely nonzero, the calculated magnetization anisotropy is still less than 0.5%. For comparison, YCo_5 has a magnetization anisotropy of order +4%, which is consistent with its MCA also being an order of magnitude larger [48].

Now considering the magnetic torque, Fig. 2(a) shows KKR-ASA calculations of $\partial F_a / \partial \theta$ for the fully-ordered magnetic state. The calculated data points (crosses) have

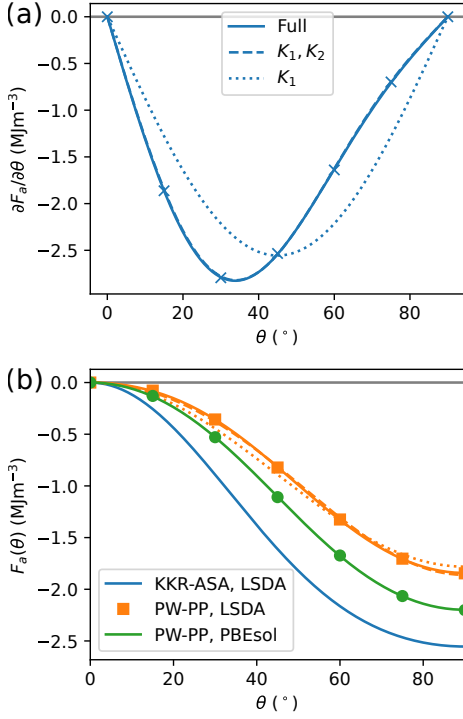


FIG. 2. The (a) magnetic torque and (b) free energy calculated at zero temperature as a function of magnetization angle θ . The symbols are calculated data points and the lines are fits to equations 1 and 5 as described in the text. The torque was calculated using the KKR-ASA approach, and equation 1 used to reconstruct the energy shown in (b). The energy zero in (b) coincides with c -axis ($\theta = 0$) magnetization.

	K_1	K_2	K_3	K_{tot}
KKR-ASA,LSDA	-3.92	1.41	-0.05	-2.56
KKR-ASA,LSDA ^a	-3.88	1.33	0.00	-2.55
KKR-ASA,LSDA ^b	-2.56	0.00	0.00	-2.56
PW-PP,LSDA	-1.16	-1.20	0.53	-1.83
PW-PP,LSDA ^a	-1.38	-0.48	0.00	-1.86
PW-PP,LSDA ^b	-1.78	0.00	0.00	-1.78
PW-PP,PBEsol	-1.96	-0.77	0.53	-2.20
Experiment [6] (4 K)	-0.37	0.37	-0.25	-0.26

^a Fit with $K_3 = 0$

^b Fit with $(K_2, K_3) = 0$

TABLE I. Zero-temperature anisotropy constants used to fit the data in Fig. 2, compared to those extracted from magnetization curves in Ref. [6]. All values are MJm^{-3} .

been fitted to the derivative of equation 1:

$$\frac{\partial F_a}{\partial \theta} = \sin 2\theta (K_1 + 2K_2 \sin^2 \theta + 3K_3 \sin^4 \theta) \quad (5)$$

Only including the K_1 term (dotted line) does not describe the calculated asymmetry of the torque around 45° . However, including K_1 and K_2 (dashed) provides an excellent account of the data. Further including K_3

(solid) represents a very small correction. The anisotropy constants extracted from the fits are given in Table I, and Fig. 2(b) shows the free energy F_a reconstructed from equation 1 using the full set of parameters.

At zero temperature, F_a is also accessible from the PW-PP formalism. In this case it is the total energy, not the torque, that is calculated, shown in Fig. 2(b). As well as the LSDA, the MCA was calculated using the PBEsol (GGA) functional [31]. The calculations were fitted to equation 1 with the K_i values given in Table I. As in Fig. 2, dotted and dashed lines are used to show the result of fitting the LSDA data to the simplified form of equation 1, where only K_1 or (K_1, K_2) were taken to be non-zero. As for the KKR-ASA case, the data is fitted very well using non-zero (K_1, K_2) only.

The different zero-temperature calculations shown in Fig. 2 all find the easy direction of magnetization to lie in the ab plane. The total MCA (K_{tot}) is shown in Table I. Its LSDA value ranges from -1.10 meV/cell (PW-PP) to -1.53 meV/cell (KKR-ASA), and the PBEsol value lies in between. A range of values have been reported in previous works, with one calculation finding -0.30 meV/cell [25] but others finding larger values like -2.2 meV/cell [26] or -2.0 [49] meV/cell, all with the LSDA. The current PBEsol calculations reproduce those reported in Ref. [20], which use the same methodology.

It is worth considering the possible origins of the difference between the two LSDA values of K_{tot} reported here. KKR-ASA is an all-electron method, providing a more complete description of the core electrons, but assumes spherical symmetry of the atomic potentials and densities. PW-PP makes no such assumption on spherical symmetry but does pseudize the core electrons. The KKR-ASA MCA is found by solving the four-component relativistic scattering problem, but the electron density remains frozen at its scalar relativistic value. By contrast, the PW-PP electron density is calculated self-consistently in two-component spin-DFT, with the relativistic effects contained in the pseudopotential [50]. Combining these factors could easily account for the observed 0.4 meV/cell (0.2 meV/FU) difference between the current LSDA results [51].

Table I does show that the individual anisotropy constants K_i exhibit greater variation between different methods compared to their sum K_{tot} . Most notably, the LSDA K_2 value has a different sign for KKR-ASA and PW-PP. However, comparing the different fits of the PW-PP LSDA data in Fig. 2(b) makes it clear that seemingly large changes in these coefficients can produce very small changes in the calculated total energy curves. The evidence for a non-zero K_2 term is much stronger based on the KKR-ASA torque curve, as seen by comparing the dotted and dashed lines in Fig. 2(a). From the phenomenological point of view, a non-zero K_2 is necessary for the easy direction of magnetization to point between the a and c axes, as discussed in the next section.

Table I also shows the anisotropy constants reported in Ref. [6] based on analysis of magnetization data. There

is an order of magnitude difference between experimental and theoretical values of K_{tot} which in absolute terms is $\sim 2 \text{ MJm}^{-3}$. This comparison emphasizes the point made in the Introduction about the effect of neglecting the coupling of the magnetism to the ionic positions. Ref. [20] found F_{vib} could account for 1 MJm^{-3} at zero temperature, and using theoretical (PBEsol) lattice constants rather than experimental ones increases F_a by 1 MJm^{-3} .

The basal plane anisotropy has also been investigated by considering the dependence of the torque and energy on the azimuthal angle ϕ when the magnetization is in the ab plane. Phenomenologically, F_a should depend on ϕ as $K_4 \cos 6\phi$ [17]. Both the KKR-ASA torque and PW-PP total energy calculations are consistent with very small values of K_4 , of order 1 kJm^{-3} . Therefore, the calculations support the experimental analysis of Ref. [6], which treated K_4 as negligible. However, the extremely small numbers calculated here are likely to be underestimates, since the anisotropy in the basal plane would be expected to be enhanced by the symmetry-lowering distortion to $Cmcm$ measured in Ref. [5].

B. Effect of hole doping on zero temperature MCA

Remaining at zero temperature, Ref. [25] previously reported that removing electrons from MnBi causes the calculated K_{tot} to switch from negative to positive. Here the KKR-ASA torque method has been used to examine this behavior in more detail, within the rigid band model. The electron number is controlled through the Fermi level μ in the Fermi-Dirac distribution function used in the calculation of the torque and integrated electron density [35]. Figure 3(a) shows the evolution of the torque as the number of removed electrons varies from -0.05 to 0.5 per MnBi unit. The calculations have been fitted to equation 5, (including the K_2 and K_3 terms) and used to reconstruct F_a , shown in Fig. 3(b). The minima of these curves (corresponding to the easy direction of magnetization) undergo a shift as electrons are removed, i.e. the material undergoes an SRT.

This SRT is seen more clearly in Fig. 3(c), which plots the easy direction against the number of removed electrons. According to the KKR-ASA calculations, removing 0.1 electrons/MnBi triggers the SRT. Removing more electrons rotates the easy direction towards the c -axis, and the SRT completes when 0.25 electrons are removed.

The extracted anisotropy constants used to construct the curves in Fig. 3(b) are shown in Fig. 3(d). The constants K_2 and K_3 fluctuate around the values obtained in the previous section (Table I), but K_1 varies strongly, going from negative to positive values. It is this variation which drives the SRT. Specifically, analyzing the stationary points of equation 1 shows the SRT will begin when the quantity $K_1 + 2K_2 + 3K_3$ switches sign from negative to positive, and end when K_1 itself becomes positive. This is confirmed in Fig. 3(d). Note that if only K_1 is nonzero, only easy angles of 0 or 90° are permitted.

This SRT was also investigated using PW-PP calculations and the LSDA. The anisotropy constants were calculated for different electron numbers and the easy angle extracted by minimizing equation 1. The results are plotted in Figs. 3(c) and (d). The PW-PP calculations predict the SRT to begin at almost exactly the same point as the KKR-ASA calculations, and to complete at only a slightly larger number of removed electrons (0.27). Given the large difference in the individual K_i values calculated with the two methods (Table I) this result is quite surprising, but as shown in Fig. 3(d) the PW-PP K_i values vary more strongly with electron number. Significantly, at the start and the end of the SRT both KKR-ASA and PW-PP find similar values for the critical quantities $K_1 + 2K_2 + 3K_3$ and K_1 . However, despite the similar start and end points the PW-PP calculations find the SRT proceeds as a rapid rotation out of plane followed by a more gradual rotation, compared to ASA-KKR where the rotation proceeds at a steady rate.

The current calculations confirm the findings of Ref. [25] and show how hole-doping brings MnBi closer to an SRT. The sensitivity to electron number indicates that there are states close to the Fermi level with competing planar/uniaxial anisotropies. It is therefore to be expected that any change the structure of the density-of-states around the Fermi level—as may occur when the unit cell volume is modified—will affect the MCA, as observed in previous studies [25, 28, 32].

C. Magnetic order at finite temperature

We now consider the calculations at nonzero temperature, using the ASA-KKR implementation of DFT-DLM to model magnetic disorder. First we focus on the magnetic order parameters m_i . It is noted above that the Mn atoms provide the dominant contribution to the magnetism at zero temperature, with the Bi atoms having a small, antiferromagnetic induced moment of $\sim 0.2 \mu_B$. This small value means that Bi atoms are unlikely to carry robust local moments, i.e. their magnitudes will go to zero once magnetic disorder is introduced [9].

To check this behavior, calculations were performed initially treating both the Mn and Bi sublattices as local moment systems. The self-consistent Weiss fields were calculated for temperatures $0 \leq T \leq 300 \text{ K}$, and the Langevin function used to obtain m_{Mn} and m_{Bi} [35]. These are plotted in Fig. 4. Focusing first on m_{Bi} , it is clear that any magnetic order associated with the Bi moments rapidly reduces as the temperature increases, with only 18% ordering at 300 K . Furthermore, the (one-shot) calculation of the local spin moment magnitude finds a significant drop, to $0.05 \mu_B$. By contrast, at 300 K the Mn atoms are 87% ordered and their spin moments remain stable at their zero temperature value, $3.82 \mu_B$. Therefore, the magnetic contribution from the Bi atoms (which was already very small at zero temperature) reduces by a further factor of 20 at 300 K .

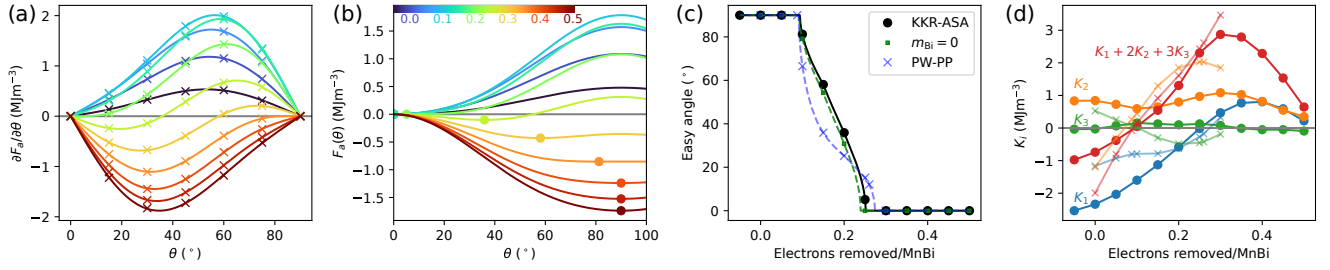


FIG. 3. The variation of the (a) magnetic torque, (b) free energy, (c) easy direction of magnetization and (d) extracted anisotropy constants, with the number of electrons removed from MnBi. In (a) and (b) the curves range from removing -0.05 (dark red) to 0.5 electrons (dark blue) in 0.05 electron intervals, with the colorbar shown in (b). The calculations have been fitted to equation 1 and the circles in (b) label the minima of the free energy curves. The data in (c) labeled $m_{\text{Bi}} = 0$ are discussed in Section III D. In (d) the data obtained from KKR-ASA and PW-PP calculations are plotted as circles and crosses, respectively. Note that the solid lines between data points in (c) were obtained by linearly interpolating the K_i values in (d) and minimizing the resulting F_a (equation 1).

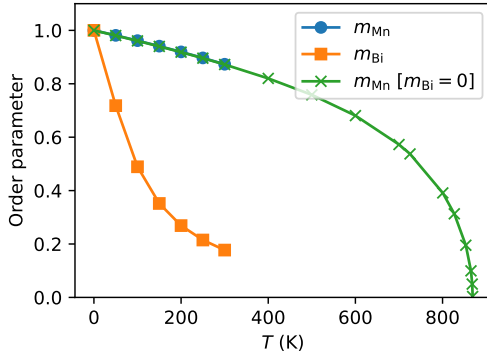


FIG. 4. The order parameters for the Mn and Bi magnetic sublattices, calculated as a function of temperature. For temperatures above 300 K the Bi order parameter m_{Bi} was set to zero. Below 300 K, calculations were performed both with $m_{\text{Bi}} = 0$ (green crosses) or finite m_{Bi} (circles/squares).

The role of the Bi moments can also be tested by forcing this sublattice to remain disordered ($m_{\text{Bi}} = 0$) at all temperatures. The order parameters of the Mn moments calculated in this way are shown as crosses in Fig. 4. Focusing on the calculations performed for $0 \leq T \leq 300$ K, we see that the values of m_{Mn} are essentially indistinguishable from the case where m_{Bi} is allowed to take nonzero values (circles). This shows that the magnetic ordering of the Mn magnetic moments is determined entirely from Mn-Mn interactions, and is independent of the state of the Bi moments. The effect that Bi ordering has on the MCA is discussed in the next section.

The Weiss fields and order parameters at the Mn sites were calculated for higher temperatures, keeping $m_{\text{Bi}} = 0$. The temperature at which the Weiss fields became vanishingly small, which is the DFT-DLM prediction of the Curie temperature T_C [35], is 870 K. The dependence of the DFT-DLM free energy on m_{Mn} is found to be well-described by a quartic expression [52], $-\frac{1}{4}J_4 m_{\text{Mn}}^4 - \frac{1}{2}J_2 m_{\text{Mn}}^2$, with J_4 and J_2 being -7 and 236 meV/atom,

respectively. Although the negative J_4 acts against magnetic ordering, its contribution is much smaller than the ferromagnetic quadratic term J_2 .

Experimentally, the Curie temperature of MnBi can only be estimated, since at 630 K the material decomposes and undergoes an abrupt transition to paramagnetism [5]. The authors of Ref. [5] fitted their magnetization data measured below the decomposition temperature to a model, $(T_C - T)^{0.28}$, which gave a value of 680 K for T_C . The DFT-DLM prediction is 200 K larger than this, but this difference is consistent with that observed in other calculations on Mn-based materials. For example, the ordering temperatures of Mn_3A compounds calculated in Ref. [52] using similar methods were found to exceed experiment by 100–500 K, depending on A. Indeed, recalling the mean-field nature of DFT-DLM, an overestimation of the Curie temperature is to be expected [35].

D. MCA at finite temperature

Having determined the dependence of the order parameters on temperature, we are now able to consider the effects of temperature on the clamped-ion MCA. Figure 5(a) shows the torque curves calculated for temperatures ranging from 0–800 K. The data have been fitted to equation 5, including all terms. Two conclusions can be drawn directly from these torque curves. First, noting that K_{tot} is equal to the area under the torque curve, Fig. 5(a) shows that the MCA is decreasing monotonically as the temperature is increased. Second, the easy angle corresponds to values of θ where $\partial F_a / \partial \theta$ is zero and its gradient is positive. Therefore, according to the data in Fig. 5(a) the easy angle remains at 90° (ab plane) at almost all temperatures. An SRT does occur, with the magnetization slightly rotating towards the c axis above 500 K. However, the system does not complete the SRT to c -axis magnetization before reaching T_C .

These conclusions are confirmed in Fig. 5(b), which

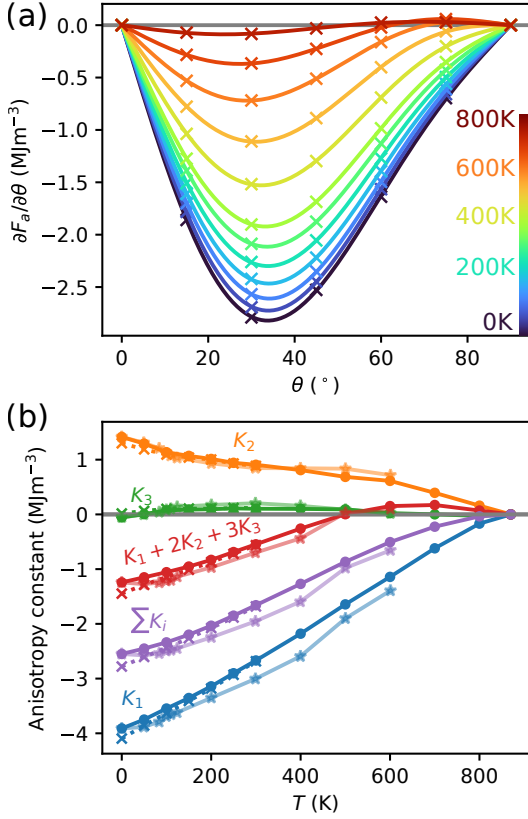


FIG. 5. (a) The magnetic torque as a function of magnetization angle θ calculated as a function of temperature from $T = 0$ K (purple) to 800 K (red). The crosses are calculated data and the straight lines fits to equation 5. (b) Anisotropy constants extracted from the fits to the torque. The circles represent points where m_{Bi} was allowed to take nonzero values below 300 K only, while the crosses represent calculations where $m_{\text{Bi}} = 0$ at all temperatures. The stars correspond to calculations performed including lattice expansion as explained in the text.

shows the anisotropy constants extracted from the fits to the torque curves. K_3 undergoes a sign change from negative to positive but remains small at all temperatures, while K_1 , K_2 and $K_{\text{tot}} (= \sum_i K_i)$ decay monotonically from their zero temperature values. The SRT begins when the critical quantity $K_1 + 2K_2 + 3K_3$ goes from negative to positive at 500 K. Numerically this occurs because the positive contribution from K_2 decays more slowly than the negative contribution from K_1 . However, because K_1 does not become positive at any temperature, the easy direction never points along the c -axis.

The data shown as circles in Fig. 5(b) were calculated assuming that the Bi moments were ordered below 300 K, according to Fig. 4. In order to test the effect of Bi order on the MCA, the torques were also calculated for the case that the Bi moments were disordered at all temperatures. The extracted anisotropy constants are shown as diagonal crosses in Fig. 5(b). At the lowest temperatures ($T \leq 100$ K) it is possible to identify differences in K_1 , e.g. of order 0.2 MJm^{-3} at $T = 0$ K. However,

above 100 K the two approaches produce indistinguishable anisotropy constants. It is therefore only the ordered Mn moments which determine the MCA at $T > 100$ K.

In light of this finding, it is interesting to repeat the zero temperature calculations of Fig. 3 assuming the Bi moments are fully disordered ($m_{\text{Bi}} = 0$) rather than ordered ($m_{\text{Bi}} = 1$). These are shown as the dashed lines/squares in Fig. 3(c). The SRT is still present, and the dependence on electron number is very similar to the $m_{\text{Bi}} = 1$ case. Therefore, even at $T = 0$ K there is little evidence to suggest that the Bi *moments* are playing a significant role in determining the MCA. However, one cannot conclude that the Bi *atoms* are unimportant, in the sense that they are an integral part of the electronic and crystal structure.

It is worth re-emphasizing that all calculations presented so far were performed for one set of lattice parameters only, measured at 4 K in Ref. [24]. However, Fig. 5(b) shows an additional set of data points (stars). For these, each data point corresponds to the lattice parameters appropriate to that temperature, as measured in Ref. [24]. Including this lattice expansion slows down the decay of the MCA with temperature. The origin of this effect is that, without including any magnetic disorder, the lattice expansion here *increases* the magnitude of the MCA, and once the two effects are combined there is a partial cancellation. For instance calculating K_{tot} at 125 K (using $c = 6.09 \text{ \AA}$) finds a value which is essentially the same as that calculated at 0 K using $c = 6.05 \text{ \AA}$; including lattice expansion has caused K_{tot} to become constant with temperature in the range 0–125 K (purple stars in Fig. 5(b)).

This finding is interesting in the context of Ref. [20]. There it was found that the rate of change of the experimental K_{tot} with temperature could be reproduced very well by considering F_{vib} alone, particularly at low temperatures. From equation 3 this would imply that F_a was constant with temperature. The authors of Ref. [20] achieved this by applying experimental thermal expansion on top of the PBEsol relaxed lattice. The results here suggest that this constant behavior could arise using experimental lattice constants only, by balancing the m and τ dependence of F_a . Incidentally, the torque calculations also show that of the different anisotropy constants, it is K_1 which varies most strongly with τ .

E. Dependence of MCA on order parameter

Returning to calculations on the $T = 4$ K lattice, in order to explore the fundamental nature of the MCA it is useful to re-plot the anisotropy constants from Fig. 5(b) as a function of order parameter m_{Mn} . To make the connection to single-ion theory the anisotropy constants are re-written in terms of the κ_l quantities using equation 2:

$$\kappa_2 = -\frac{2}{3}K_1 - \frac{16}{21}K_2 - \frac{16}{21}K_3$$

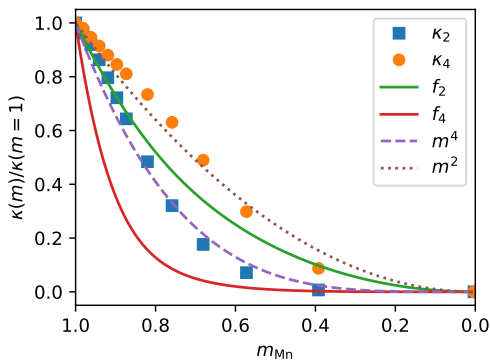


FIG. 6. The anisotropy constants κ_2 and κ_4 (equation 2) extracted from Fig. 5(b) and plotted as a fraction of their zero temperature values versus order parameter. The expected decay due to single-ion theory (f_2 and f_4) or to simple power laws are also shown.

$$\begin{aligned}\kappa_4 &= \frac{8}{35}K_2 + \frac{144}{385}K_3 \\ \kappa_6 &= -\frac{16}{231}K_3\end{aligned}\quad (6)$$

In single-ion theory these quantities decay with order parameter according to $\kappa_l(m) = \kappa_l(m=1)f_l(m)$, where $\kappa_l(m=1)$ is the zero temperature value and $f_l(m)$ are functions which depend on m as $m^{l(l+1)/2}$ and m^l in the limiting cases of low and high temperature [10]. Therefore, a central prediction of this theory is that the highest-order (largest l) κ_l values decay the fastest.

Figure 6 shows the decay of κ_2 and κ_4 relative to their zero temperature values. Straightaway, a challenge is presented to single-ion theory, since κ_4 decays more slowly with m than κ_2 . κ_6 presents an even more severe challenge, which can be seen from equation 6 and Fig. 5(b): κ_6 is proportional to K_3 , and K_3 does not decay monotonically with temperature, but in fact switches sign. Given the smallness of K_3 and the good fit of the torque data using only K_1 and K_2 , it is likely κ_6 is more susceptible to numerical noise. Certainly, the calculated κ_6 cannot be described by any monotonic function.

Figure 6 also shows the single-ion decay functions $f_2(m)$ and $f_4(m)$, and the simple power laws m^4 and m^2 . For the order parameter range 1.0–0.87 ($0 \leq T \leq 300$ K), κ_2 is rather well-described by f_2 . As the temperature is further increased, the calculated κ_2 is better described by m^4 , which is outside the limiting $m^3 \rightarrow m^2$ behavior of f_2 . κ_4 decays far more slowly. The single-ion prediction f_4 decays as m^{10} at low temperatures, but the rate of decay of the calculated κ_4 values is in fact slower than m^2 . Empirically, the decays of κ_2 and κ_4 can be described at a similar level of accuracy using the simple m^4 and m^2 power laws respectively.

Given that MnBi is a metal, whose magnetism originates from itinerant electrons rather than isolated single ions, it is not surprising that Fig. 6 does not show general agreement between the DFT-DLM calculations and

single-ion theory. The model analysis recently presented in Ref. [14] argued that itinerant ferromagnets with spin and orbital degrees of freedom could have κ_2 exhibiting power law behavior outside the single-ion limits of $m^3 \rightarrow m^2$ as observed here. Arguably, the more surprising aspect is the apparent success of f_2 in describing κ_2 over a reasonably large temperature range.

The current calculations highlight the complex behavior of the higher order anisotropy constants. In particular, the slow decay of κ_4 means that it continues to play a role even at high temperature, which is not expected from single ion theory. Indeed, although the spin-model calculations of Ref. [12] were able to provide a good overall account of the anisotropy of MnBi, the study found that the experimentally reported K_2 values were not well described using only single-ion terms, with the latter decaying too quickly. The current calculations provide an empirical basis for introducing additional terms which decay more slowly. However, no attempt is made here to provide a rigorous theoretical justification (e.g. in the form of a microscopic Hamiltonian) for such terms.

IV. SUMMARY AND OUTLOOK

This study has used first-principles calculations based on DFT to study the magnetocrystalline anisotropy of MnBi, focusing on the effect of magnetic disorder. The zero temperature results have been cross-validated using two different implementations of DFT, namely within the KKR-ASA (Green's function) or PW-PP (wavefunction) approaches. The KKR-ASA calculations at zero temperature found total magnetic moments of $3.95 \mu_B$ for the Mn atoms, consisting of 3.82 and $0.13 \mu_B$ spin and orbital contributions respectively, with a 0.5% reduction in magnetization when rotated from the a to c axis. This value is in good agreement with the $3.90(2) \mu_B$ value measured from neutron diffraction [5]. At zero temperature the Bi atoms show magnetic moments which are antiferromagnetically aligned to Mn, with spin and orbital contributions of 0.15 and $0.03 \mu_B$.

Raising the temperature causes a rapid disordering of the Bi moments and a drop in spin moment magnitude to $0.05 \mu_B$ at 300 K, showing that these cannot be considered robust local moments. By contrast, the Mn spin moment is unchanged at 300 K and the moments remain 87% ordered. The calculations demonstrate that the Mn ordering is unaffected by the state of the Bi moments. The calculated Curie temperature is 870 K, whose overestimation of the experimentally-derived value of 680 K [5] is consistent with other studies on Mn-based systems using similar methodology [52].

Calculations of the anisotropy energy at zero temperature find an in-plane easy direction with $K_{\text{tot}} = -2.56$ or -1.83 MJm^{-3} using the KKR-ASA or PW-PP approaches, respectively. The angle-resolved data show clear evidence of a nonzero K_2 term but the additional correction from K_3 is relatively small. The individual

anisotropy constants show larger differences between the KKR-ASA and PW-PP approaches, most notably in the sign of K_2 . However, both approaches agree that removing 0.1 electrons from MnBi induces a spin reorientation transition, leading to c -axis magnetization once 0.25–0.27 electrons have been removed. The calculations also find negligible anisotropy within the ab plane ($\sim 1 \text{ kJm}^{-3}$).

Using the KKR-ASA implementation of the disordered local moment picture to model finite temperature magnetic disorder, the magnitude of the total MCA K_{tot} is found to reduce monotonically with temperature. The easy magnetization direction remains in the ab plane until 500 K when it begins to rotate towards the c -axis, but the SRT does not complete before the Curie temperature is reached. The ordering of the Bi moments only has a small influence on the anisotropy constants below 100 K and is negligible otherwise.

The κ_2 and κ_4 anisotropy constants decay monotonically with temperature (decreasing order parameter). In the temperature range $0 \leq T \leq 300 \text{ K}$, κ_2 follows the decay expected from single ion theory [10] but undergoes a faster m^4 decay at higher temperatures. By contrast, κ_4 decays more slowly than predicted by single ion theory, as approximately m^2 . κ_6 does not follow a monotonic decay with order parameter. It is hoped that the data presented here on the m -dependence of κ_2 and κ_4 may be useful to theorists aiming to elucidate fundamental mechanisms of anisotropy in itinerant magnets.

The calculations finding a monotonic decay of K_{tot} were performed at fixed lattice parameters. When lattice expansion was considered, the decrease in the magnitude of K_{tot} due to magnetic disorder was partly offset by an increase in its zero temperature value as the lattice parameters evolved. As a result, K_{tot} remained at a constant value over the temperature range 0–125 K once thermal expansion was included.

The main result of this study is to rule out magnetic disorder as the sole explanation for the temperature dependence of the MCA in MnBi. If the lattice parameters are held fixed, no SRT is observed at low temperatures and K_{tot} remains negative and decays to zero, which is at odds with experimental observation. However, a quantitative theory of the MCA of MnBi should not neglect magnetic disorder, particularly at higher temperatures where κ_2 exhibits the m^4 decay. It was noted in the Introduction that previous theoretical works [20, 26] were able to reproduce the experimental K_{tot} to an impressive level of accuracy up to 450 K. However, at higher temperatures the calculations did not reproduce the experimentally-observed peak and subsequent drop in K_{tot} . Referring to equation 3, including the m dependence would restore the peak, since all anisotropy would disappear in the $m = 0$ limit. The current study has quantified the m -dependence of F_a .

Determining the m -dependence of F_{vib} is an unresolved and highly interesting problem. Already, calculating F_{vib} for $m = 1$ and $\theta = 0$ and 90° is a significant technical accomplishment [32] which has been implemented in PW-

PP calculations. However, the DFT-DLM formalism simulates magnetic disorder within the CPA, which is naturally implemented in the Green's function-based KKR-ASA framework but not in PW-PP. Very recent work replacing the CPA with configurational averaging over constrained magnetic states has allowed DFT-DLM calculations to be performed in a wavefunction-based framework at fixed ionic positions [53], whilst phonon calculations on the paramagnetic state have also been demonstrated [21, 22]. Furthermore, supercell approaches provide easier access to anharmonic effects, as demonstrated in Ref. [54] which also accounted for the effects of partial magnetic ordering on interatomic forces. On the other hand, DFPT allows a very fine sampling of phonon frequencies in reciprocal space, which is necessary to obtain a converged value of F_{vib} . Understanding the interplay between lattice dynamics and MCA is increasingly under investigation [55] and likely to undergo further interesting progress in the near future.

Another issue which needs to be resolved to obtain a *predictive* theory of the MCA based on DFT is the exchange-correlation functional. Here, it was shown that the difference between the MCA calculated within the LSDA or using the PBEsol functional was quite small, 0.4 MJm^{-3} , when using the same lattice parameters. However, if the lattice parameters are found by minimizing the total energy, the LSDA dramatically underestimates the c -parameter (by 8%), with PBEsol slightly better (6%) [20], and calculating the MCA at these structures greatly amplifies the difference. Adding a U correction can produce lattice parameters closer to experiment [30], but depending on how the U value is chosen this reduces the predictive element [56]. These different choices—the exchange-correlation functional, experimental or optimized lattice parameters, including a U correction—all affect the calculated MCA, whose experimental value is small (-0.26 MJm^{-3} , or -0.16 meV/cell [6]). Also, the most widely-used relativistic DFT total energy expressions do not include the dipole-dipole contribution to the MCA, which was found to be 0.16 MJm^{-3} in Ref. [12].

Although the description of the MCA of MnBi presented here is already rather complex, it is worth remembering that it assumes the stoichiometric NiAs structure. Apart from not accounting for the low temperature distortion discussed in Sec. II A, the current description does not consider the possible role played by defects or an off-stoichiometric composition [57]. Given the sensitivity of the MCA to the Fermi level position, this would be an important consideration, especially for understanding practical magnets grown in different conditions.

Based on the findings of this study it is suggested that the MCA of MnBi should really be treated as two phenomena: the low temperature SRT, and the subsequent increase of K_{tot} . For the SRT, it is possible that the Bi moments may play a minor role, and based on the experimental measurements of the crystal structure, it seems unlikely that magnetostriction can be ignored.

However, the effects of magnetic disorder are relatively small in the low temperature regime. For the increase of K_{tot} at higher temperatures, the disappearing induced moments on Bi means that the description should focus on the MCA generated by the Mn moments. The lattice parameters do vary smoothly in this regime, although the possibility of thermally-activated defects should be considered. However, magnetic disorder becomes increasingly more important due to the m^4 dependence, and is required to explain the peak in K_{tot} at 460 K.

ACKNOWLEDGMENTS

This work was carried out with the support of a Royal Society Research Grant RGS\R1\201151. The author would like to acknowledge the use of the University of Oxford Advanced Research Computing (ARC) facility in carrying out this work [58].

Appendix A: Protocol for determining Wigner-Seitz radii

In the atomic sphere approximation (ASA), space is partitioned into overlapping atom-centred spheres whose volumes add up to that of the unit cell. Within these spheres, the potential and charge density is taken to be spherically symmetric. Additional basis freedom can be provided by introducing empty spheres. The NiAs structure (Fig. 1) contains clear voids at the $2d$ sites which are obvious candidates for empty sphere sites. Denoting the Wigner-Seitz radii of spheres centred on the Mn, Bi and empty sites as r_{Mn} , r_{Bi} and r_{E} , we are left with the question of what sizes these radii should be. Two radii can be considered free parameters, and the third is constrained by the ASA total volume condition.

Different methods have been proposed to choose these parameters, e.g. Ref. [59]. The procedure used here takes the density ρ calculated in the PW-PP approach, which makes no spherical approximation. Spherical averages of the density $\bar{\rho}$ are then constructed by interpolating the density onto a polar (r, θ, ϕ) Lebedev grid [60]

$$\bar{\rho}(r) = \frac{1}{4\pi} \int \sin\theta d\theta d\phi \rho(r, \theta, \phi) = \frac{1}{4\pi} \sum_i w_i \rho(r, \theta_i, \phi_i) \quad (\text{A1})$$

where w_i are the Lebedev weights, and r is linearly spaced between 0 and 4 Bohr radii. The mean square value $\bar{\rho}^2(r)$ is calculated in the same way, and the deviation obtained as $\sigma_X^2(r_X) = \bar{\rho}_X^2(r_X) - [\bar{\rho}_X(r_X)]^2$ where X labels a particular atom. Then, the set of radii $\{r_{\text{Mn}}, r_{\text{Bi}}$ and $r_{\text{E}}\}$ are found which minimize $\sigma_{\text{Mn}}^2(r_{\text{Mn}}) + \sigma_{\text{Bi}}^2(r_{\text{Bi}}) + \sigma_{\text{E}}^2(r_{\text{E}})$, subject to the ASA total volume constraint. In the tests considered here this protocol always led to a unique set of radii.

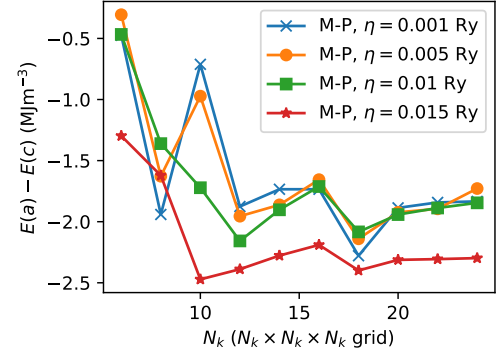


FIG. 7. Convergence of the energy difference between a and c -axis magnetization with reciprocal space sampling, for various values of the Methfessel-Paxton (M-P) smearing width η .

Appendix B: Influence of the electronic temperature and smearing scheme

In the DFT-DLM scheme, quantities like the torque are calculated as integrals over energy, of the form $-1/\pi \text{Im} \int dE f_{\text{FD}}(E, \mu, T_{\text{el}}) F(E)$ [35]. Usually, T_{el} is treated as a fixed parameter, used to aid convergence by smearing out k -point integrations [35]. However, one could also argue that it is a physical temperature, which affects the occupation of electronic states around the Fermi level μ through the Fermi-Dirac function f_{FD} , and therefore should match T , i.e. the temperature associated with the magnetic disorder.

Technically, reducing T_{el} introduces a new challenge because a denser k -point grid is required to converge the reciprocal space integrals. Whilst the adaptive algorithm [43] alleviates this issue for the DFT-DLM part of the calculation, the generation of the frozen potentials in the SCF KKR-ASA part becomes prohibitively expensive. For this reason, the electronic temperature T_{el} was fixed to 300 K throughout this work.

Some justification for this approach is provided by the PW-PP calculations. Here, the electronic states are occupied according to the Methfessel-Paxton (M-P) scheme, which ideally tends to the $T_{\text{el}} = 0$ limit [47]. Using the first-order M-P scheme implemented in **Quantum ESPRESSO**, the only variable is the smearing width η , which in turn affects the number of k -points required to achieve convergence of the reciprocal space integral.

Figure 7 demonstrates this convergence, focusing on the difference in energy between a and c -axis magnetization. The two calculations' Fermi energies display qualitatively similar convergence behavior. Although choosing a value for η of 0.015 Ry can lead to a result which apparently converges with the number of k -points, reducing η to 0.01 Ry leads to a 20% reduction in the calculated anisotropy energy. However, further reducing η does not induce any further change, so we can be reasonably confident that the $\eta=0.01$ Ry values used in this work do

represent the zero temperature limit. Now we return to the KKR-ASA calculations presented in Fig. 3(c). Here, the approach of fixing T_{el} to 300 K led to very close agreement with the PW-PP calculations regarding the onset of the SRT. If we accept the reliability of the PW-PP calculations, this is a point in favor of the $T_{\text{el}} = 300$ K approach.

It is worth noting that although the PW-PP calcu-

tions are numerically converged with η and k -points, the first-order M-P scheme is itself an approximation. A full assessment of different reciprocal space smearing techniques and their impact on anisotropy energies is beyond the scope of this study. However, Fig. 7 does emphasize the importance of DFT-based studies on metallic magnets paying attention not just to the k -point sampling but also to the electron occupation scheme.

-
- [1] R. R. Heikes, Phys. Rev. **99**, 446 (1955).
 - [2] J. Coey, Scripta Mat. **67**, 524 (2012).
 - [3] A. Andresen, W. Halg, P. Fischer, E. Stoll, G. Eriksson, R. Blinc, S. Paušak, L. Ehrenberg, and J. Dumanović, Acta Chem. Scand. **21**, 1543 (1967).
 - [4] T. Hihara and Y. Kōi, J. Phys. Soc. Japan **29**, 343 (1970).
 - [5] M. A. McGuire, H. Cao, B. C. Chakoumakos, and B. C. Sales, Phys. Rev. B **90**, 174425 (2014).
 - [6] W. E. Stutius, T. Chen, and T. R. Sandin, AIP Conf. Proc. **18**, 1222 (1974).
 - [7] For completeness, it should be noted that a small number of studies found the SRT to occur differently, with MnBi showing easy cone magnetization at 4 K and only a gradual rotation to the c axis observed; see Ref. [61] and references therein.
 - [8] C. Kittel, Rev. Mod. Phys. **21**, 541 (1949).
 - [9] B. L. Győrfy, A. J. Pindor, J. Staunton, G. M. Stocks, and H. Winter, J. Phys. F: Met. Phys. **15**, 1337 (1985).
 - [10] H. Callen and E. Callen, J. Phys. Chem. Solids **27**, 1271 (1966).
 - [11] M. D. Kuz'min and A. M. Tishin, Handbook of magnetic materials (Elsevier B.V., 2008) Chap. 3, p. 149.
 - [12] J. Barker and O. Mryasov, J. Phys. D: Appl. Phys. **49**, 484002 (2016).
 - [13] J. B. Staunton, S. Ostanin, S. S. A. Razee, B. L. Győrfy, L. Szunyogh, B. Ginatempo, and E. Bruno, Phys. Rev. Lett. **93**, 257204 (2004).
 - [14] D. Miura and A. Sakuma, J. Phys. Soc. Japan **91**, 023706 (2022).
 - [15] S. Kumar, C. E. Patrick, R. S. Edwards, G. Balakrishnan, M. R. Lees, and J. B. Staunton, J. Phys.: Condens. Matter **32**, 255802 (2020).
 - [16] S. Hirose, Y. Matsuura, H. Yamamoto, S. Fujimura, M. Sagawa, and H. Yamauchi, J. Appl. Phys. **59**, 873 (1986).
 - [17] J. J. M. Franse and R. J. Radwański, Handbook of magnetic materials (Elsevier North-Holland, New York, 1993) Chap. 5, p. 307.
 - [18] J. F. Herbst, Rev. Mod. Phys. **63**, 819 (1991).
 - [19] S. Baroni, S. de Gironcoli, A. Dal Corso, and P. Giannozzi, Rev. Mod. Phys. **73**, 515 (2001).
 - [20] A. Urru and A. Dal Corso, Phys. Rev. B **102**, 115126 (2020).
 - [21] F. Körmann, B. Grabowski, B. Dutta, T. Hickel, L. Mauger, B. Fultz, and J. Neugebauer, Phys. Rev. Lett. **113**, 165503 (2014).
 - [22] D. Gambino and B. Alling, Phys. Rev. B **98**, 064105 (2018).
 - [23] Y. Choi, P. J. Ryan, M. A. McGuire, B. C. Sales, and J.-W. Kim, Appl. Phys. Lett. **112**, 192411 (2018).
 - [24] J. B. Yang, Y. B. Yang, X. G. Chen, X. B. Ma, J. Z. Han, Y. C. Yang, S. Guo, A. R. Yan, Q. Z. Huang, M. M. Wu, and D. F. Chen, Appl. Phys. Lett. **99**, 082505 (2011).
 - [25] A. Sakuma, Y. Manabe, and Y. Kota, J. Phys. Soc. Japan **82**, 073704 (2013).
 - [26] V. P. Antropov, V. N. Antonov, L. V. Bekenov, A. Kutepov, and G. Kotliar, Phys. Rev. B **90**, 054404 (2014).
 - [27] K. V. Shanavas, D. Parker, and D. J. Singh, Sci. Rep. **4**, 7222 (2014).
 - [28] V. N. Antonov and V. P. Antropov, Low Temp. Phys. **46**, 1 (2020).
 - [29] A. N. Yaresko, V. N. Antonov, and P. Fulde, Phys. Rev. B **67**, 155103 (2003).
 - [30] N. A. Zarkevich, L.-L. Wang, and D. D. Johnson, APL Mater. **2**, 032103 (2014).
 - [31] J. P. Perdew, A. Ruzsinszky, G. I. Csonka, O. A. Vydrov, G. E. Scuseria, L. A. Constantin, X. Zhou, and K. Burke, Phys. Rev. Lett. **100**, 136406 (2008).
 - [32] A. Urru and A. Dal Corso, Phys. Rev. B **100**, 045115 (2019).
 - [33] J. P. Perdew and A. Zunger, Phys. Rev. B **23**, 5048 (1981).
 - [34] P. Strange, H. Ebert, J. B. Staunton, and B. L. Győrfy, J. Phys.: Condens. Matter **1**, 2959 (1989).
 - [35] C. E. Patrick and J. B. Staunton, Electron. Struct. **4**, 017001 (2022).
 - [36] H. Ebert, D. Ködderitzsch, and J. Minár, Rep. Prog. Phys. **74**, 096501 (2011).
 - [37] P. Giannozzi *et al.*, J. Phys.: Condens. Matter **21**, 395502 (2009).
 - [38] J. B. Staunton, L. Szunyogh, A. Buruzs, B. L. Győrfy, S. Ostanin, and L. Udvardi, Phys. Rev. B **74**, 144411 (2006).
 - [39] S. H. Vosko, L. Wilk, and M. Nusair, Can. J. Phys. **58**, 1200 (1980).
 - [40] M. Dane, M. Luders, A. Ernst, D. Ködderitzsch, W. M. Temmerman, Z. Szotek, and W. Hergert, J. Phys.: Condens. Matter **21**, 045604 (2009).
 - [41] X. Wang, R. Wu, D.-s. Wang, and A. J. Freeman, Phys. Rev. B **54**, 61 (1996).
 - [42] A. Oswald, R. Zeller, P. J. Braspenning, and P. H. Dedrichs, J. Phys. F: Met. Phys. **15**, 193 (1985).
 - [43] E. Bruno and B. Ginatempo, Phys. Rev. B **55**, 12946 (1997).
 - [44] A. Deák, E. Simon, L. Balogh, L. Szunyogh, M. dos Santos Dias, and J. B. Staunton, Phys. Rev. B **89**, 224401 (2014).
 - [45] A. Dal Corso, Comput. Mater. Sci. **95**, 337 (2014).
 - [46] H. J. Monkhorst and J. D. Pack, Phys. Rev. B **13**, 5188 (1976).
 - [47] M. Methfessel and A. T. Paxton, Phys. Rev. B **40**, 3616

- (1989).
- [48] J. M. Alameda, D. Givord, R. Lemaire, and Q. Lu, J. Appl. Phys. **52**, 2079 (1981).
 - [49] P. Ravindran, A. Delin, P. James, B. Johansson, J. M. Wills, R. Ahuja, and O. Eriksson, Phys. Rev. B **59**, 15680 (1999).
 - [50] A. Dal Corso, Phys. Rev. B **82**, 075116 (2010).
 - [51] It could also be noted that the KKR-ASA and PW-PP calculations use different LSDA parameterizations, Refs. [39] and [33] respectively, although given the high accuracy of these parametrizations this is an unlikely source of the discrepancy.
 - [52] E. Mendive-Tapia and J. B. Staunton, Phys. Rev. B **99**, 144424 (2019).
 - [53] E. Mendive-Tapia, J. Neugebauer, and T. Hickel, Phys. Rev. B **105**, 064425 (2022).
 - [54] M. Heine, O. Hellman, and D. Broido, Phys. Rev. B **100**, 104304 (2019).
 - [55] G. Xing, Y. Miura, and T. Tadano, Phys. Rev. B **105**, 104427 (2022).
 - [56] There is also a question whether the dependence of the energy on magnetization angle found with LSDA+ U and reported in Ref. [26] can be successfully described with equation 1.
 - [57] K. Anand, J. Pulikkotil, and S. Auluck, J. Magn. Magn. Mater. **363**, 18 (2014).
 - [58] <http://dx.doi.org/10.5281/zenodo.22558>.
 - [59] O. Jepsen and O. K. Andersen, Z. Phys. B **97**, 35 (1995).
 - [60] V. Lebedev and D. Laikov, Dokl. Math. **59**, 477 (1999).
 - [61] J. B. Yang, W. B. Yelon, W. J. James, Q. Cai, M. Kornecki, S. Roy, N. Ali, and P. l'Heritier, J. Phys.: Condens. Matter **14**, 6509 (2002).